

Linear attenuation of water and real-time imaging of capillary rise in soil

Mähring, Marcus¹

¹ETH Zürich
December 3, 2021

Abstract

This experiment aimed to teach the basics of neutron imaging, the concepts which facilitate the technique, some applications thereof, as well as shine a light on the challenges which arise in association thereto. As a part of the process, the linear attenuation of water was determined by imaging different depths of water using a neutron beam at the NEUTRA beamline at PSI. These images were compensated for using open beam correction methods, ultimately delivered results of μ between $(1.10 \pm 0.01) \text{ cm}^{-1}$ up to $(1.698 \pm 0.010) \text{ cm}^{-1}$, whereas the expected value was at 2.5 cm^{-1} . Using black body correction gave values between (2.196 ± 0.151) and $(3.123 \pm 0.034) \text{ cm}^{-1}$, which was still small in relation to the expected corrected attenuation coefficient of 3.6 cm^{-1} . The second part of the experiment determined the average pore size of three different sand samples, between $r = (0.510 \pm 0.030) \mu\text{m}$ and $(4.91 \pm 0.34) \mu\text{m}$ for the different samples. It was planned to extract the average water per pixel in the imaging, but was not possible to be done due to a technical error at NEUTRA's neutron source.

Contents

1	Introduction	4
1.1	The goal of the experiment	4
1.1.1	Why neutrons?	4
1.1.2	Beer-Lambert's law	4
1.1.3	Washburn's equation	5
1.2	Scintillators	5
2	Experiment	7
2.1	NEUTRA and the SINQ beamline	7
2.2	Setup and general procedure	7
2.3	Notes on calibration and scattering contributions	8
2.3.1	Focusing the camera and determining pixel size	8
2.3.2	Correcting for scattered neutron and noise	9
2.4	Determining the linear attenuation coefficient for water	10
2.4.1	Black body correction	12
2.5	Validation of Washburn's equation	12
2.5.1	Sample preparation	12
2.5.2	Observing the capillary rise	12
2.5.3	Notes on the completeness of the experiment	13
3	Results	14
3.1	Linear attenuation of water	14
3.2	Black body corrections	14
3.3	Validity of Washburn's equation	16
4	Data analysis	17
4.1	Image preprocessing	17
4.2	Evaluating the quality of the data	17
5	Discussion	18
5.1	Linear attenuation of water	18
5.1.1	Linear attenuation coefficient with open beam normalization	18
5.1.2	Black body scattering correction	20
5.1.3	Determining the scattering correction images	20
5.1.4	Linear attenuation coefficient using black body calibration	22
5.2	Washburn's equation and determining pore size	24
6	Conclusion	27

A Safety	28
A.1 Controlled zones in PSI	28
A.2 Safety procedure when initiating the beam	28
A.3 Dangers inherent in the setup	28

1 Introduction

1.1 The goal of the experiment

The general goal of this experiment is to experimentally determine the linear attenuation coefficient of water and confirming the Washburn equation by way of observing capillary rise in sand [1]. Neutron imaging, which is used for the experiment, has widespread applications in materials science and sciences concerning themselves with investigation of water contents. In the following section a short introduction to neutron imaging and the measurement technique is given, thereafter a description of the experimental setup and procedure are presented, and finally the results are discussed.

1.1.1 Why neutrons?

A central concept which endorses the method of neutron imaging is its sensitivity to low Z elements; elements with a low amount of particles in its core. In our experiment we wish to sample a relatively fast process as accurately as possible, i.e. recording as clear a difference as possible between the wet and dry parts of our samples. Using neutron imaging thus a good choice, as it will easily penetrate the containers and samples, while quickly registering any water in our samples [1].

1.1.2 Beer-Lambert's law

For a beam of neutrons with initial intensity I_0 the measured intensity I after attenuating in a medium is given by Beer-Lambert's law:

$$I = I_0 \exp \left[- \int \mu(x) dx \right] \quad (1)$$

Here the intensity of the neutron beam after traveling a distance x in the material is dependent on $\mu(x)$, the linear attenuation coefficient. This is a measure of how much of the beam is scattered/absorbed per unit of thickness in the material. In imaging experiments, one can use open beam correction, which compensates for certain biases in the equipment and in the beam [1] [2].

$$\int \mu(x) dx = - \log \left(\frac{D_0}{D} \frac{I - I_{DC}}{I_0 - I_{DC}} \right) \quad (2)$$

Here I_{DC} is a measurement acquired without the beam, giving the background signal/noise of the experiment, it is also known as the dark current bias of the camera. Subtracting this from the all our images effectively removes the inherent background from the camera equipment (see section 2). Additionally, we normalize the images with the open beam measurements. The quotient D_0/D is the quotient of the open beam dose and D the dose

taken in the image of the measurement. A dose is here defined to be the average image intensity of a region not covered by the specimen. This gives a compensation for flux fluctuations and vibrations in the beam which generate imperfections in the beam [1][2].

When considering the total attenuating effect between just before and after the sample, one must also include the effect of the soil itself and the container. To determine the water content from a single frame one then uses:

$$I_{\text{Wet}} = I_0 \exp [-(L_{H_2O}\mu_{H_2O} + L_{\text{Soil}}\mu_{\text{Soil}} + L_{\text{Container}}\mu_{\text{Container}})]$$

Likewise, we expect a dry sample to follow the same form but without any water therein.

$$I_{\text{Dry}} = I_0 \exp [-(L_{\text{Soil}}\mu_{\text{Soil}} + L_{\text{Container}}\mu_{\text{Container}})]$$

Computing the fraction of $I_{\text{Wet}}/I_{\text{Dry}}$, one gets:

$$L_{H_2O}\mu_{H_2O} = -\log \left(\frac{I_{\text{Wet}}}{I_{\text{Dry}}} \right)$$

This is the optical thickness of the water, from which one can find the metric fitness by determining the linear attenuation coefficient of water.

1.1.3 Washburn's equation

The equation governing capillary rise was determined in the early 1900's by Washburn:

$$L = \sqrt{\frac{\gamma r t \cos(\phi)}{2\eta}} \quad (3)$$

More exactly the equation describes the depth L a fluid with surface tension γ and viscosity η penetrates into a capillary as a function of time. Additionally, it considers the impact of the average pore size r and the contact angle ϕ of the liquid in the capillary. In our case $\gamma = 72 \times 10^{-3}$ N/m, $\eta = 0.89$ mPa s, and $\phi = 50^\circ$ [3].

This equation has some limiting factors, mainly in regions where intertial forces and dynamic contact angle effects play a significant role [4].

1.2 Scintillators

Scintillation detectors (scintillators) are some of the most prevalent particle detectors in physics today. They have several desirable quantities; they are sensitive to the energy of the particles and additionally have a fast response time. Their working principle uses the fact that when struck, certain materials emit light and aim to maximize this effect with

materials that have as clear of a reaction as possible while having a high cross-section in relation to the particle one wishes to measure. This facilitates the experiment described in this article as scintillators are used to convert the neutrons into photons, which can be detected to a high degree of accuracy with a high-quality camera [5] [3].

Scintillators are often made of so-called luminescent material, i.e. material which emits energy taken from some source as visible light. If reemission occurs within 10^{-8} s (the time for atomic transition) we call it fluorescent. If the reemission happens later than this or during a longer period, one refers to *afterglow*. This can last on a timescale from $\sim 1\mu\text{s}$ up to hours depending on the material. [5].

The scintillator in this experiment, ^6Li is one such material, where the afterglow lasts about 10 minutes, which must be considered when taking calibration data sets, to avoid light-contamination of the references – especially of the dark reference. ^6Li is chosen because of its high scattering cross-section with neutrons: > 70 [3]. Another alternative would have been ^{10}Br , as both are sensitive to β, γ radiation [5].

2 Experiment

2.1 NEUTRA and the SINQ beamline

The experiment was performed at the Swiss Spallation Neutron Source (SINQ). A spallation neutron source exploits accelerated ion's collisions with a target to produce neutrons. At SINQ this is achieved via a cyclotron which accelerates ions and collides them into such a target after which they are mediated by deuterium / heavy water to produce specific types of neutron beams, achieving a neutron flux of 10^{14} n/(cm²s) [6].

The experiment station used was the NEUtron TRAnsmission RAdiography station (NEUTRA). The NEUTRA line specializes in non-invasive analysis of hydrogenous materials akin to tissue plastic and water. At NEUTRA, the neutron flux is slightly lower than the production at SINQ: about 10^7 n/(cm²s). The spectrum heavily favours thermal neutrons (see figure 1): free neutrons with energy corresponding to the mode of the Maxwell-Boltzmann distribution. This is useful, as they have a large effective neutron absorption cross-section [7].

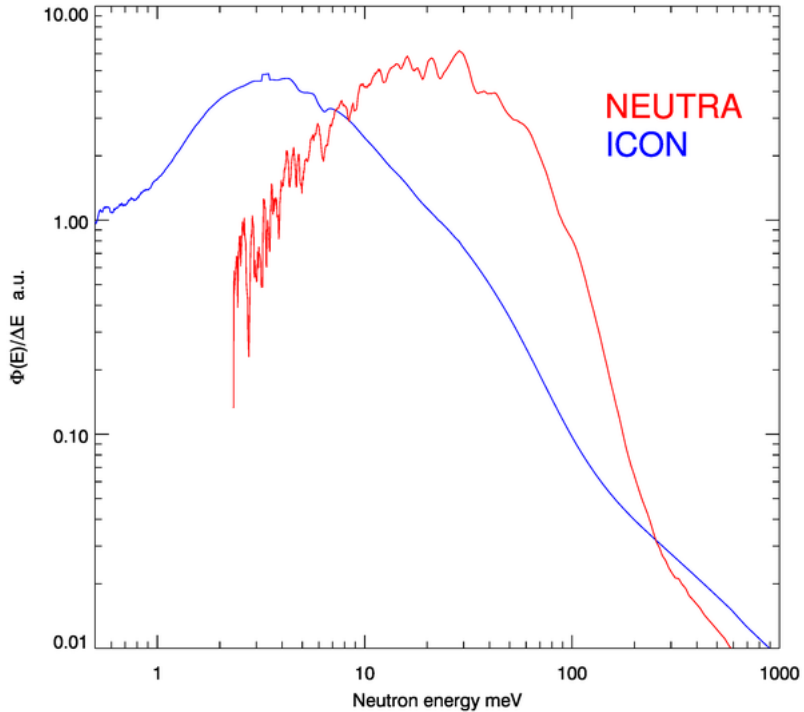


Figure 1: The energy - flux plot of two neutron imaging experiment lines at SINQ. Note how the flux of NEUTRA is heavily focused in the thermal spectrum [7].

2.2 Setup and general procedure

The setup consisted of a platform in front of the neutron source on which one could place the sample to image. The platform was motorized, and was as such able to be moved remotely. Following the sample, a ⁶Li scintillator was mounted. Finally a mirror reflects

the produced light from the scintillator into the camera above. The camera was set to a focal length of 0.5 m and was cooled to -30°C to reduce thermal noise. The exact focal length of the camera was not set directly, as there was some minimal displacement (about 23 mm) coming from the position of the camera's focus in relation to the scintillator (distance from the scintillator to the mirror); the granularity of the scale of the camera's focus was insufficient for this calibration, so to increase accuracy and avoid this error source, additional calibration was performed (see the following section). See figure 2 for a graphical representation of the setup.

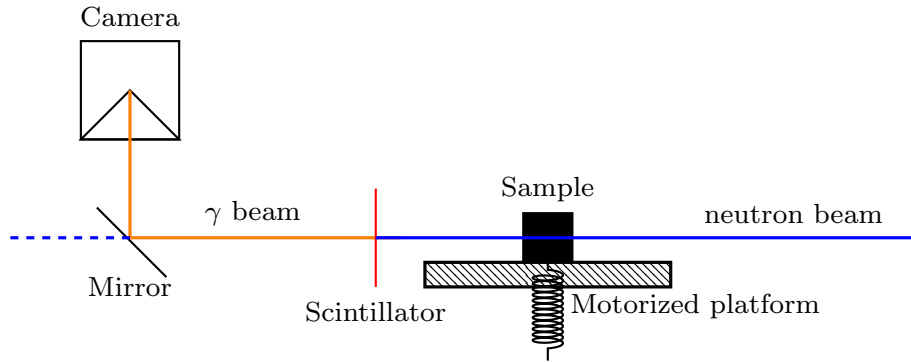


Figure 2: A schematic of the setup with the main components and the beams. This image is not to scale.

2.3 Notes on calibration and scattering contributions

2.3.1 Focusing the camera and determining pixel size

To ensure focus on the camera's focus. An aluminum plate, in practice invisible to the neutrons, with Gd details. Gadolinium has a very significant attenuation of neutrons, meaning these details on the plate will be very clearly visible. Thus if the pattern on the plate is clearly visible, then the camera is well calibrated. The plate also had increments, grids and ranges from parts of a millimeter up to a centimeter. In figure 3 the photo of the plate, taken with the experiment, at which point the camera was calibrated is displayed; it was subsequently used to determine the pixel size.

Every grid square on the grid placed over the entire plate, as seen in figure 3, corresponds to one centimeter. This enables us to determine the size of one pixel on the pictures of the calibrated camera. Note that the position of the sample on the position is unimportant, as the calibration of the camera only relates to the position of the camera in relation to the scintillator.

To more precisely determine the pixel size, the grid lines needed to be determined to as high an accuracy as possible. Accentuating the lines can be done with an edge detection algorithm, for instance the canny edge detection algorithm. In figure 4 a zoomed in seg-

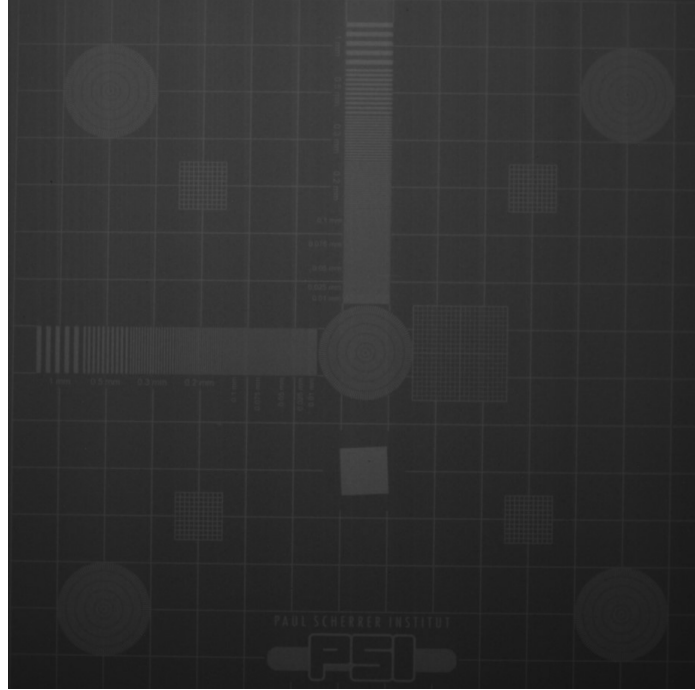


Figure 3: The plate (black) with Gd details, which appear as white. Zoomed in a fine resolution reveals itself, which can be further enhanced with edge detection algorithms.

ment of the calibration image from figure 3 treated with such an edge detection algorithm (Gaussian kernel 1 with the a lower threshold of 0.1 and upper threshold of 2.5) is shown. Measuring the distance of 14 cm with an insignificant error, due to the high fabrication quality of the calibration plate. The distance in pixels gave the length (1578 ± 1) px, meaning we have a conversion factor of (112.72 ± 0.07) px/cm, or equivalently we have (88.716 ± 0.056) $\mu\text{m}/\text{px}$.



Figure 4: The result of applying the canny edge detection algorithm with Gaussian kernel 1 with the a lower threshold of 0.1 and upper threshold of 2.5 on a subset of figure 3.

2.3.2 Correcting for scattered neutron and noise

An important note for the setup as described above has an important bias for which one should compensate to improve accuracy. The attenuation on the neutron beam resulting from the water is highly dependant on the scattering cross section of hydrogen, meaning

that neutrons are scattered in the sample and hardly absorbed. Thus, the non-scattered neutrons which miss the sample or pass by without scattering contribute to a bias in the experiment when they hit the scintillator. The photons produced in this interaction will may be directly be scattered unto the camera, leading to abnormal bright spots, but the primary problem is that the uncollided neutrons still contribute to the brightness, leading to an underestimate of the attenuation. In figure 5 an illustration thereof is displayed [8].

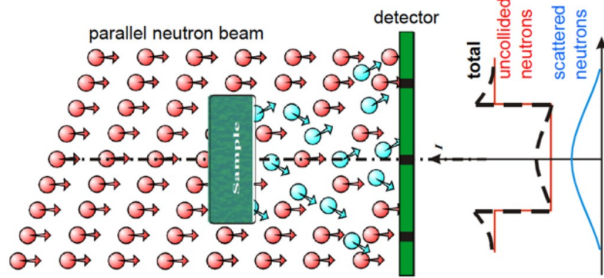


Figure 5: Neutron beam scattering on a material. Observe the two distributions / plots on the right-hand side, and note how the total distribution overestimates the scattered neutrons [1].

This can be removed by imaging a so called black-body grid (bb) of Gd. A grid of small spheres of Gd placed in front of the sample, which works as additional calibration. This enables one to remove the background from the beam scattering and other background noise, e.g. containers for the sample or similar. A more thorough description of the process can be found in [2] [8]. In figure 6 the modified setup with the additional element is displayed along with an example of back scattering.

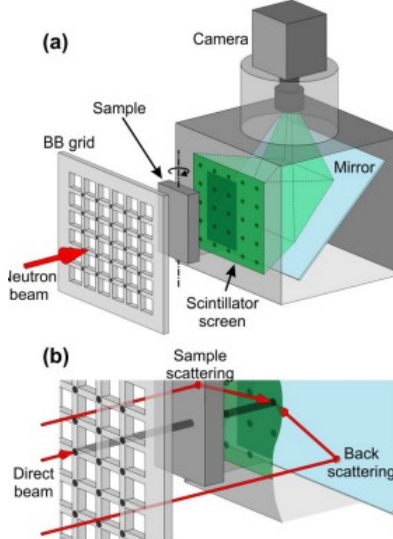


Figure 6: An illustration of a potential bb setup with an explicit example for the back scattering of unscattered neutrons [8].

2.4 Determining the linear attenuation coefficient for water

To determine the attenuation coefficient of water three step wedges, containers with depth varying along their height, were placed with tape with adhesive on each side onto a board

to keep them in place. One of the step wedges had the depths 0.5 mm to 2.5 mm in 0.5 mm steps (far left in figure 7) with the other two having the interval 3.0 mm to 5.0 mm with the same step length as before. The images were taken with 2s exposure time with full resolution in batches of about 5-10 and were averaged to decrease noise.



Figure 7: The three step wedges. Far right the step wedge with the increments 2.5 mm to 0.5 mm and the two on the right both have depths between 5.0 mm and 3.0 mm

For calibration purposes the following images were taken: (1) dark current, (2) open beam, (3) images with the empty step wedges, (4) an image with black bodies, (5) images with the black bodies in front of filled wedges, and finally (6) normal images with the filled wedges. These images are shown in figure 8. The dark current images were taken first, as to avoid bias due to the scintillator afterglow.

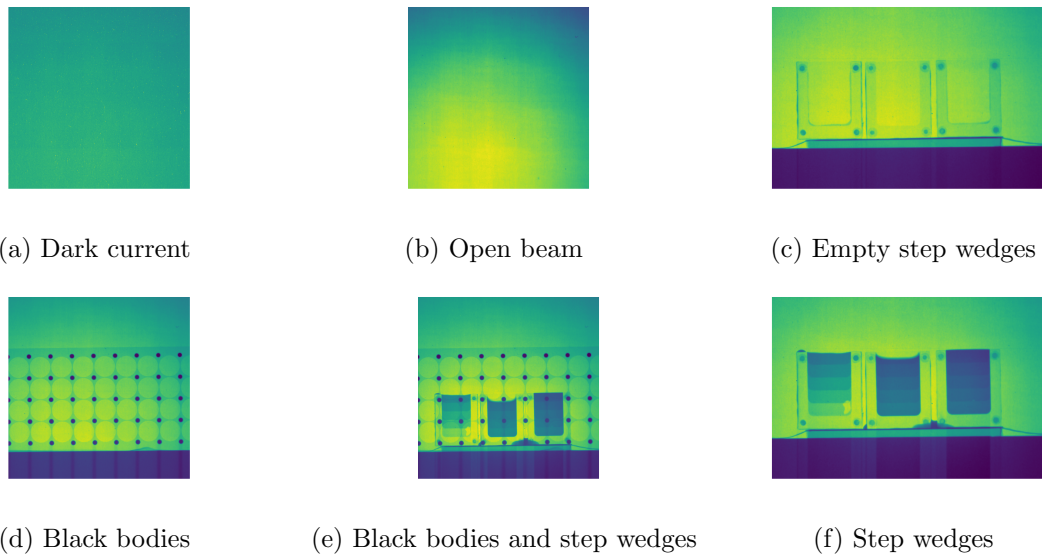


Figure 8: Samples of the taken images for the different categories.

The dark current and open beam images are as described in section 1 an image of the

background without beam and one of just the beam with no sample, respectively. These were mainly there to compensate for oscillations in the beam and background noise of the equipment.

2.4.1 Black body correction

By considering the black body correction we more precisely assume our data has the form:

$$I_{\text{Measured}} = I_{\text{Sample}} + I_{\text{Scattering Component}} + I_{\text{DC}}$$

$$I_{\text{OB measured}} = I_{\text{OB}} + I_{\text{Background Scattering}} + I_{\text{DC}}$$

Here I_{Measured} is the measured quantity from the experimental setup. DC and OB is as before the dark current/open beam. $I_{\text{Scattering Component}}$ is an interpolated expression for an expected scattering component and $I_{\text{Background Scattering}}$ is a measurement of the background scattering of the camera system (the unscattered neutrons). The quantity to be determined is I_{Sample} and I_{OB} , which should be uninfluenced by the backscattering.

This leads one to the normalization scheme [2]:

$$I_N = \frac{I_{\text{Measured}} - I_{\text{DC}} - I_{\text{Scattering Component}}}{I_{\text{OB measured}} - I_{\text{DC}} - I_{\text{Background Scattering}}} \cdot \frac{D(I_{\text{Measured}} - I_{\text{DC}} - I_{\text{Scattering Component}})}{D(I_{\text{OB measured}} - I_{\text{DC}} - I_{\text{Background Scattering}})}$$

Here I_N is the image which is normalized with the black body scattering and ready for analysis. This analysis – as mentioned – using equation (2) to determine $\mu \cdot x$, the optical depth of the water in the sample.

2.5 Validation of Washburn's equation

2.5.1 Sample preparation

Firstly, the samples of sand needed to be prepared. For this experiment to work, a bottom of the sand container had to be permeable to water. This was achieved by gluing a think film to the bottom of the containers with a glue gun. Then the containers were filled with sand. This was done by filling the containers with sand of different grain sizes varying from 0.1 mm to 3.2 mm. The different combinations of grain size and the range of different grain sizes in the different samples are displayed in figure 9.

2.5.2 Observing the capillary rise

To observe capillary rise the samples were mounted onto an elevated point above the motorized platform. Then a time series of 200 pictures (3 s per picture) was started. After a few images the platform was raised remotely so that the water just came into contact with the lower part of the container, allowing capillary rise to occur. Images



Figure 9: The different planned samples. The far left were plastic beads while the four rightmost are mixes of sand in different ranges and of differing sizes. Note the white tissue-like cloth under the containers: the water-permeable membrane.

were taken with a time interval between and 2 s and 3 s. This would have taken much longer, due to the camera processing the images after they were taken and not in parallel. To accelerate the process, a binning of 2x2 (bundling pixels together and summing their values) and a smaller size. To counteract the de facto quadrupling of the brightness values, the exposure time was quartered – 0.5 s – in comparison with the last part, where the exposure time was set at 2 s.

2.5.3 Notes on the completeness of the experiment

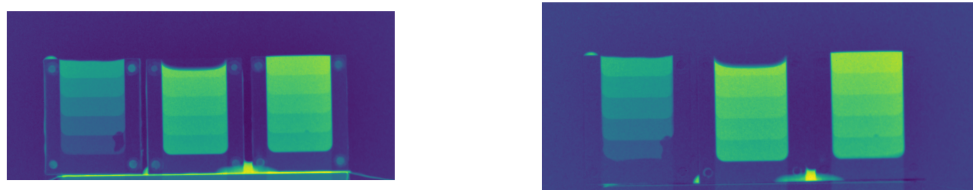
Some complications arose at the end of the beam-time due to a cooler on an injector malfunctioning, cutting the experiment short. Firstly this meant that only the samples for sand 2 (0.1 mm – 0.2 mm), 3 (0.1 mm – 3.2 mm), and 4 (0.4 mm – 0.8 mm) could be taken. Additionally, this meant that the data in these cases lacked bb-references and open beam images.

3 Results

3.1 Linear attenuation of water

From the reference / calibration images as shown in figure 8 a simple open-beam correction can be done. Once using the pure open beam (figure 8b), which can be seen in figure 10a, and one removing the step wedges (figure 8c), in turn displayed in figure 10b. Note how in the latter figure, the outline of the container edges are no longer distinctly visible, while this is still a factor in the image where just the background was subtracted.

Another thing which stands out on these pictures is that one of the step wedges was leaking. This can be seen by the additional bright spot between the two rightmost step wedges. If this is cut out correctly when doing the analyses this is of no concern, but one should be attentive to the fact that this might contribute as a false signal later, if it satisfies a certain mask (absorbs a certain amount of neutron), but is in a false position in relation to the rest of the data.



(a) Image of the filled step wedges calibrated using the open beam.

(b) Image of the filled step wedges calibrated using just the empty step wedges.

Figure 10: Two ways to perform open beam correction. Left the correction is performed with the open beam and right with the empty step wedges.

Below (figure 11) are some sample slices from the different step wedges and how the averaging of the intensity values at the respective depths (0 - 500 px). Note how there are intervals where the optical depth remains constant. This corresponds to the regions of images where the depth of the step wedge remained constant, and is as such uninteresting. The slopes observed are of interest, as the slope of the line they represent is the linear attenuation coefficient. Note how the parts with the most water have the highest optical thickness, and are as such situated in the leftmost part of each step wedge image.

3.2 Black body corrections

The black body corrections calculated using the given library gave images as displayed in figure 12. In the right image, the correction for the grid and the step wedges is shown.

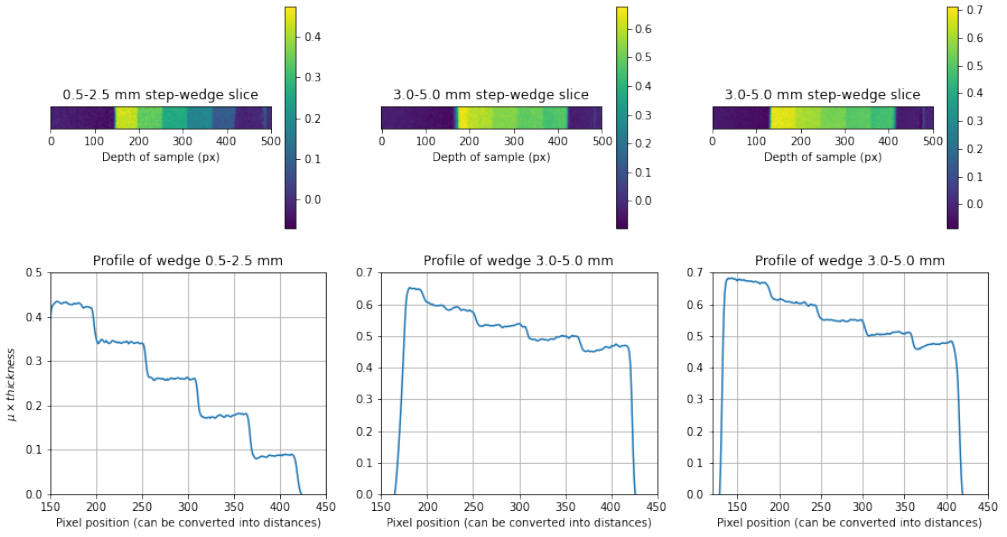


Figure 11: The three step wedges average optical depth at different distances into the material. The constant segments represent the areas where the depth is constant, while the intermediary parts give the transition to the new depth. On the y-axis the optical depth is displayed in arbitrary units, and on the x-axis we have the distance into the sample in px. Note how this is not particularly relevant, as we know the width of the step wedges and that the highest optical depth should be where the sample is the thickest, i.e. at 2.5 mm and 5.0 mm respectively (compare with equation (1)).

The images are flipped to be upright, and one can clearly see how the lower part of the experiment, where many neutrons fly past the sample, has a high correction factor. In contrast, the outer parts, where the image gets more similar to the open beam images, the correction diminishes greatly. Analogously, in the scattering correction for the open beam and the bb grid, small corrections are needed around the grid itself, and for the neutrons missing the target in the lower right, where they are not removed by calibration.

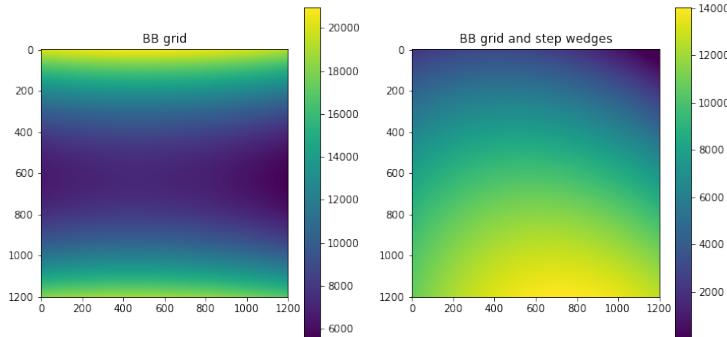


Figure 12: The scattering corrections for just the bb grid (left) and the grid together with the filled step wedges (right).

3.3 Validity of Washburn's equation

After submerging the lower edge of the container's in water capillary rise quickly started, and a time series of images was taken with about 2-3 second intervals. An example of one such frame for the third sample can bee seen in figure 13. In every image one can clearly recognize the platform, the aluminum bath and the water therein. The additional along the sides and top of the container is the aluminum tape used to affix the sample for dunking it in the bath.

Of particular interest is of course the water surface propagating through the sample. This can be seen as a smoke-like dark effect in each sample.

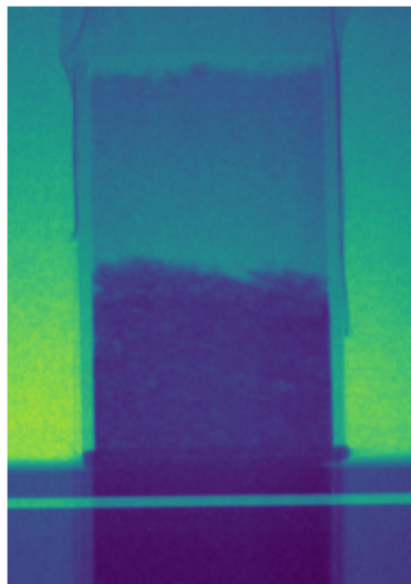


Figure 13: The 18'th frame (42 s after starting) of observing the sample 3 (grain size 0.1 mm – 3.2 mm).

4 Data analysis

4.1 Image preprocessing

Another error which may occur on the basis of the equipment is that the scintillator sometimes emits an additional γ during scintillation. If this photon hits the camera directly, parts of the image will have spikes in brightness. To mitigate this in images with a high amount of such imperfections a smoothing filter can be applied to remove such point-like imperfections. However, one should make sure that the smoothing is localized if sharpness of the image's edges at some points is important.

In determining the linear attenuation, this particular error source was compensated for by always using the average over a minimum of five images. In the case such imperfections are very unlikely to occur.

In the part of the experiment where we are concerning ourselves with the validity of the Washburn equation, without filtering, this could however become an error source as one could overestimate the position of the water front. To this end, the pore sizes are also calculated using the average height of the water column.

4.2 Evaluating the quality of the data

For these kinds of imaging experiments, the SNR is most aptly defined regionally where one compares the average signal in a region to the standard deviation of the region [9], see equation (4).

$$\text{SNR} = \frac{\mu[\cdot]}{\sigma[\cdot]} \quad (4)$$

In this equation $\mu[\cdot]$ and $\sigma[\cdot]$ is the mean and the standard deviation for the image region $[\cdot]$ respectively.

5 Discussion

5.1 Linear attenuation of water

In Carminati et al., [2], the expected linear attenuation of water, when compensating for back-scattering at the NEUTRA beamline is quoted to be about 3.6 cm^{-1} . When not compensating, one should expect about 2.5 cm^{-1} [3].

5.1.1 Linear attenuation coefficient with open beam normalization

With normalized images one can identify all points where the derivative is small relative the others. To a certain degree of error, this will give us the eligible points which indicate the optical depth of the sample. In a first step, the derivative need be plotted together such that a mask can be obtained. With this mask one can now find the points dividing the data set between the different sections corresponding to their respective physical depths. An example of such an analysis is given in figure 14.

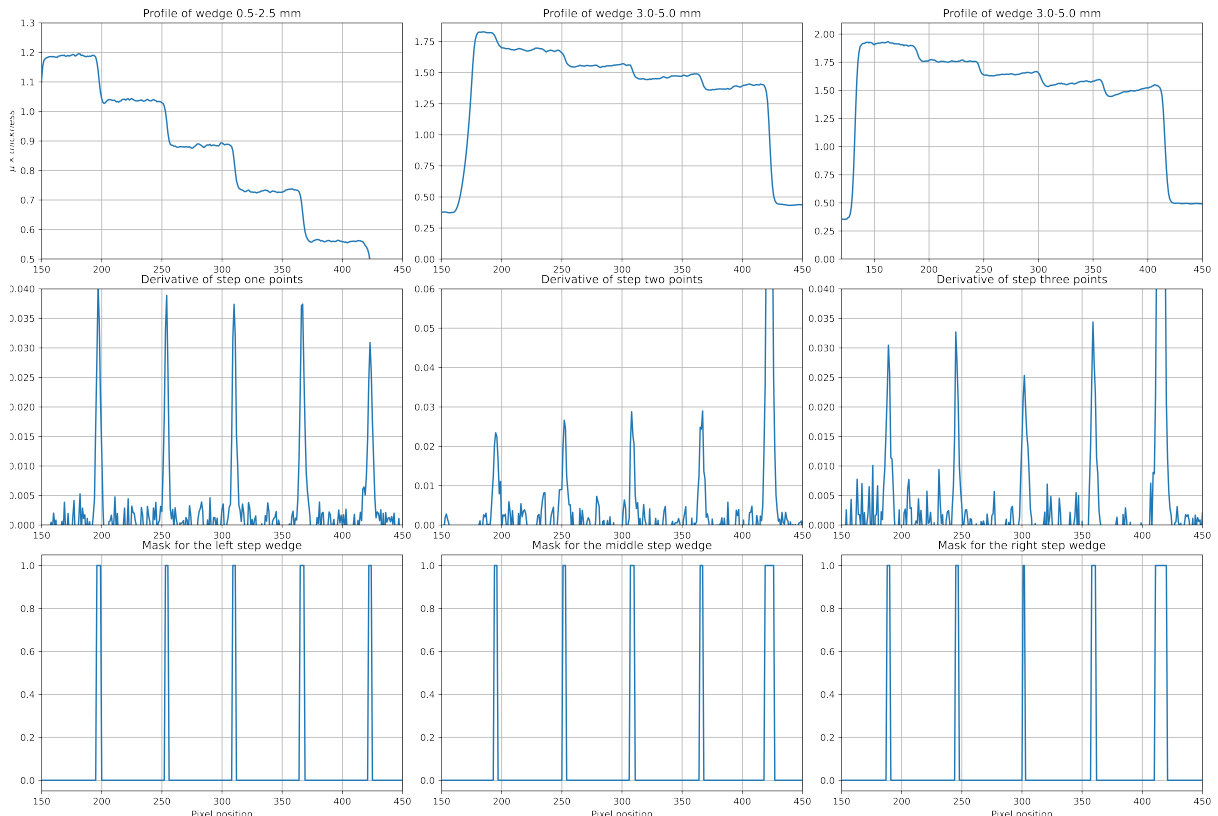


Figure 14: The step wedge plots and their approximated derivatives (first two rows respectively). From the derivatives of the step wedges we can identify the interfaces between the optical depths and creating a mask (last row).

From the determined cutoff points determined in the paragraph above, we can find the points in the original graph corresponding to a certain width of the step wedge. This is shown in figure 15, with the different colors indicating which part of the sample the optical depth.

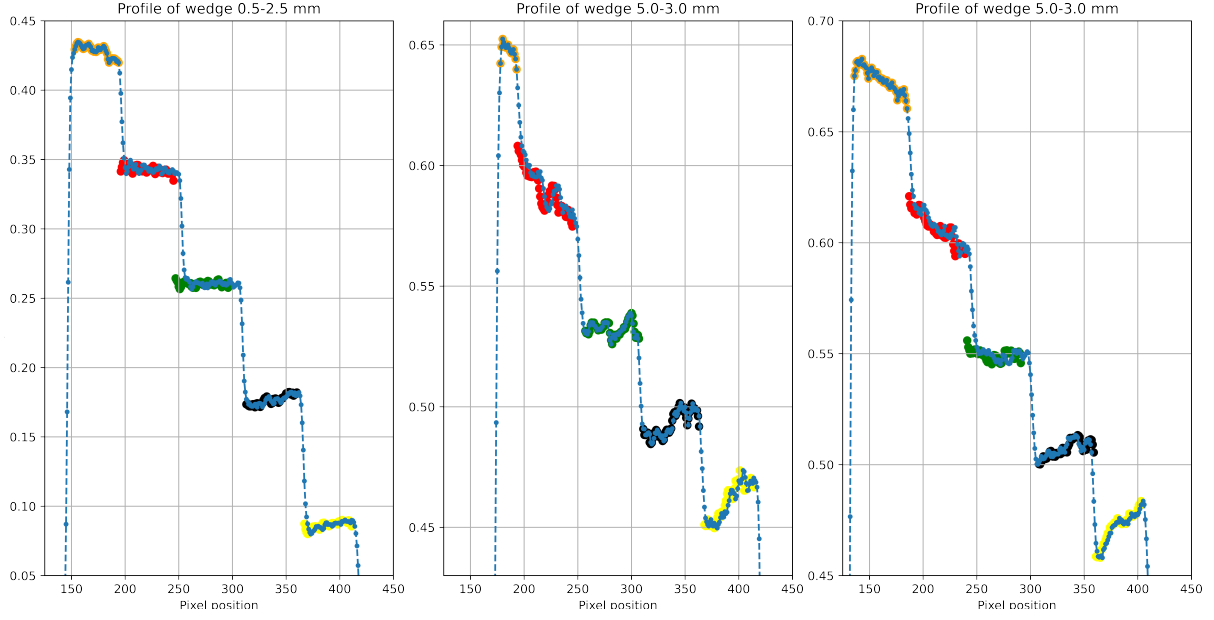


Figure 15: The image used to find the explicit points of each width of the step wedges with the colors indicating the depth (orange to yellow is on a linear scale with decreasing depth). These points are later used to calculate the average optical depth per width of the step wedges.

To calculate the linear attenuation coefficient, one only needs to recognize that [1]:

$$L_{\text{Optical}} = \mu L_{\text{Physical}} + \delta_{\text{err}}$$

With δ_{err} an added factor to compensate for possible errors in the variables. Thus, by fitting this one can extract μ . The fitted values for the step wedges with two different open beam calibrations (one with just the open beam, and once with the empty step wedges) are given in table 1.

	Open beam	Empty containers
$\mu_{2.5}^{\text{left}}$	$(1.698 \pm 0.010) \text{ cm}^{-1}$	$(1.671 \pm 0.013) \text{ cm}^{-1}$
$\mu_{5.0}^{\text{mid}}$	$(1.573 \pm 0.303) \text{ cm}^{-1}$	$(1.657 \pm 0.357) \text{ cm}^{-1}$
$\mu_{5.0}^{\text{right}}$	$(1.036 \pm 0.107) \text{ cm}^{-1}$	$(1.100 \pm 0.086) \text{ cm}^{-1}$

Table 1: Linear attenuation coefficients when normalizing with an open beam and with just the empty step wedges.

One interesting note here is that we expect the empty containers to be a marginally more accurate representation of the actual attenuation coefficient as they also take the material's depth into consideration. That the values differentiate themselves so little, at the second decimal place, one can conclude that the aluminum has a minimal impact on the neutron beam. This is also supported by previous research [1].

These values for the linear attenuation as given in 1 is significantly smaller than expected. A possible reason for this is that the uncertainty for the average optical depth of the samples was quite high for all measurements. This means when one performs a weighted

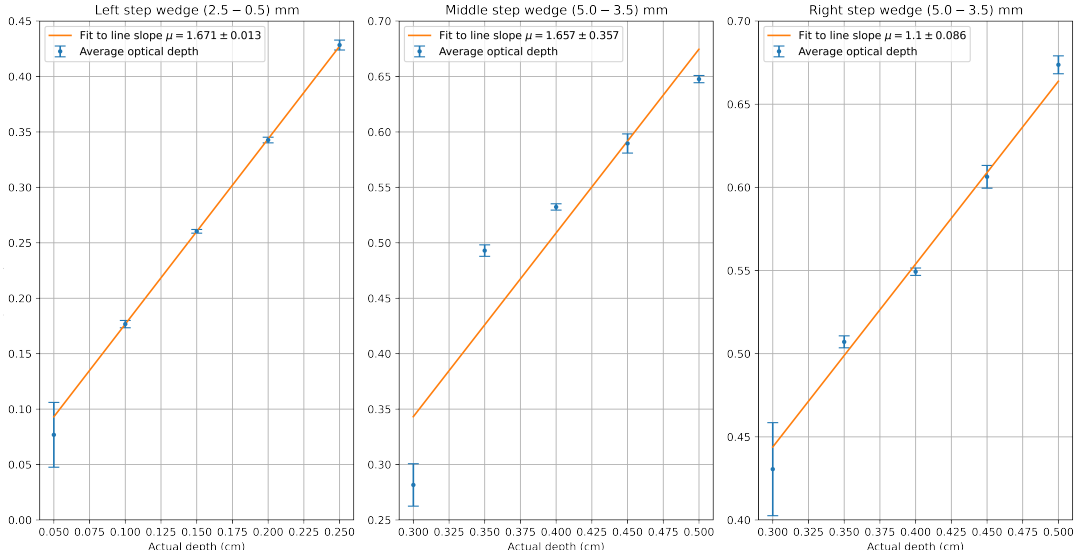


Figure 16: Fits to the data for the empty step wedge normalization. Note that we fit to five points, as we only know the actual physical depth for five regions in the image

fit, the first point, which accounts for the majority of the slope in especially the second and third wedges (example given for the empty step wedge normalization in image 16).

That this error was significantly larger than any other value could originate from noise as the optical depth of these parts were the closest to the background, and the platform. Thus some of the platforms values might have gotten included in the data cleaning and analysis.

5.1.2 Black body scattering correction

5.1.3 Determining the scattering correction images

This section describes how the scattering images from figure 12 were computed. Firstly a cutoff value to create a mask for finding the bbs was found by converting the images to one-dimensional arrays. When plotting these as a histogram – see figure 17 – we expect a peak describing the general counts in the image, but with the bb grid, we expect an additional one for the black bodies.

The black bodies are hardly permeable for neutrons, we expect these to have a very dark color in the images. Thus, we conclude that the first peak must be (among other things) the black bodies, and choose a cutoff value accordingly.

Note how due to the variety of channels in the image with the sample, i.e. the different optical depths of the water contribute to the area between the two peaks. Thus, in the left histogram, there are very few points in the intermediary space between the beam brightness and the black bodies; this is visible in the left histogram, but in the right this space is filled with the channels from the optical depths of the filled step wedges.

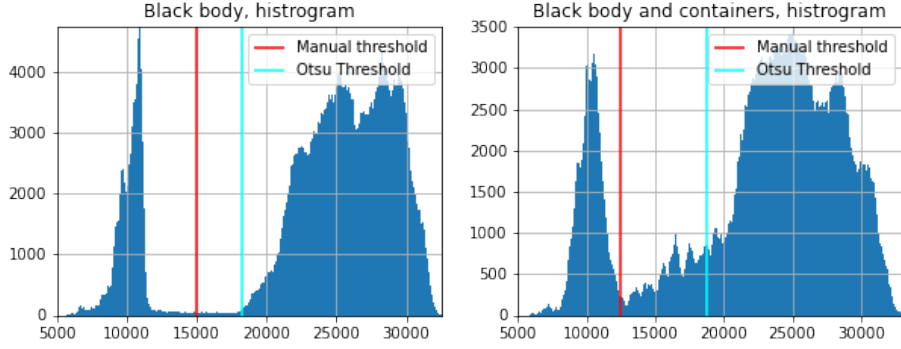
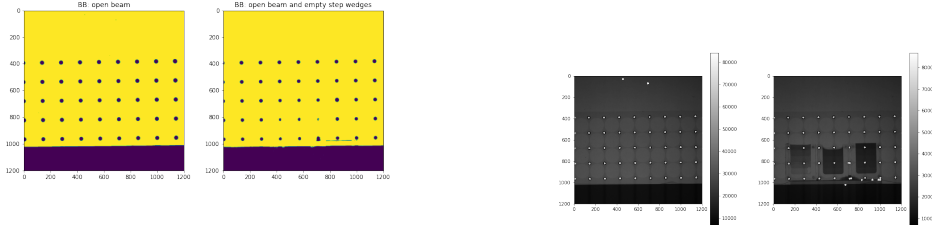


Figure 17: The figure shows the histograms for the two black body images. On the left, the histogram for just the black bodies is given, and on the right is the image for the black bodies and the filled step wedges. In both images a manual approximation of where the bb channels end and the Otsu threshold are plotted as vertical lines. Note how the Otsu segments the image too generously, especially in the right image the filled step-wedges get interpreted as black bodies.

After this, the threshold was checked by displaying the original images masked with the condition that the image should be greater than the determined threshold value. This gave the images in 18a. In this image it is interesting to note how the poor separation between the peaks in the histogram for the BBs and the sample leads to noise in the mask where some bbs are smaller than others and additional noise appearing near the platform (solid dark block).

Subsequently, with this information one could explicitly find the coordinates for the black bodies using a mask. In figure 18b an example on how this could look like is given. Now one uses an algorithm from the positions of the black bodies and their radii to calculate the scattering correction image. Due to the noise seen in 18b, some additional corrections will be added to the scattering correction, but as they are relatively minimal or close to other grid points, it was assessed that they would have a minimal impact on the scattering correction.



- (a) The masks identifying the points dark enough to qualify as black bodies. The black bodies are then separated from the platform – by means of an algorithm which considers the size of a circle overlaid over the objects.
- (b) Black bodies (white spots) identified using the mask generated in the previous stage. Here one should note how the images both include a certain amount of noise, but especially the one with the filled step wedges.

5.1.4 Linear attenuation coefficient using black body calibration

When using BB correction the sample came out as shown in figure 19. Note how the color in the entire image are much more subdued in comparison with the previous instances and how the background in the entire image is very close to zero.

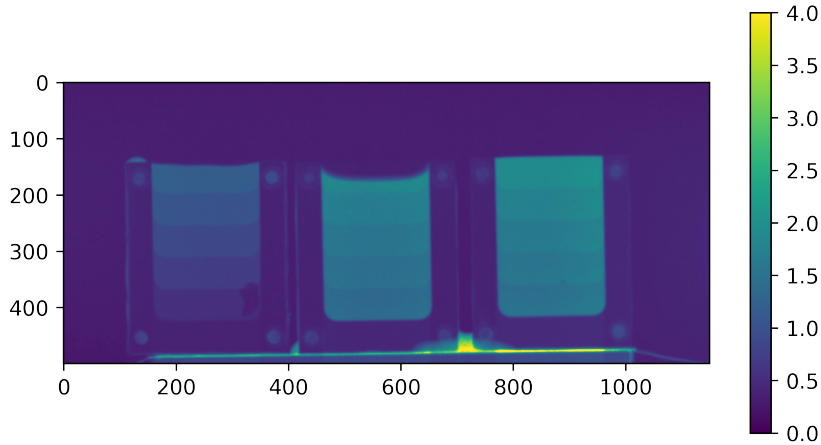


Figure 19: The step wedge images after using black body correction, note how the background is completely filtered out and how the leaking water indeed acts as an error source which should be filtered out before engaging in the analysis of the optical depth.

Now, using the argumentation as described for the open-beam normalized images, we can fit linear functions to the new data sets. This is displayed in figure 20 and the values for the fits are given in table 2.

One should note that this is still about 1 cm^{-1} below the expected value. This could be explained by the fact that in [2] an additional factor between 0 and 1 was introduced to rescale the corrected image. This is still unaccounted for here.

	Left step wedge	Middle step wedge	Right step wedge
$\mu [\text{cm}^{-1}]$:	(3.123 ± 0.034)	(2.196 ± 0.151)	(2.231 ± 0.241)

Table 2: The corrected attenuation coefficients calculated for the different step wedges.

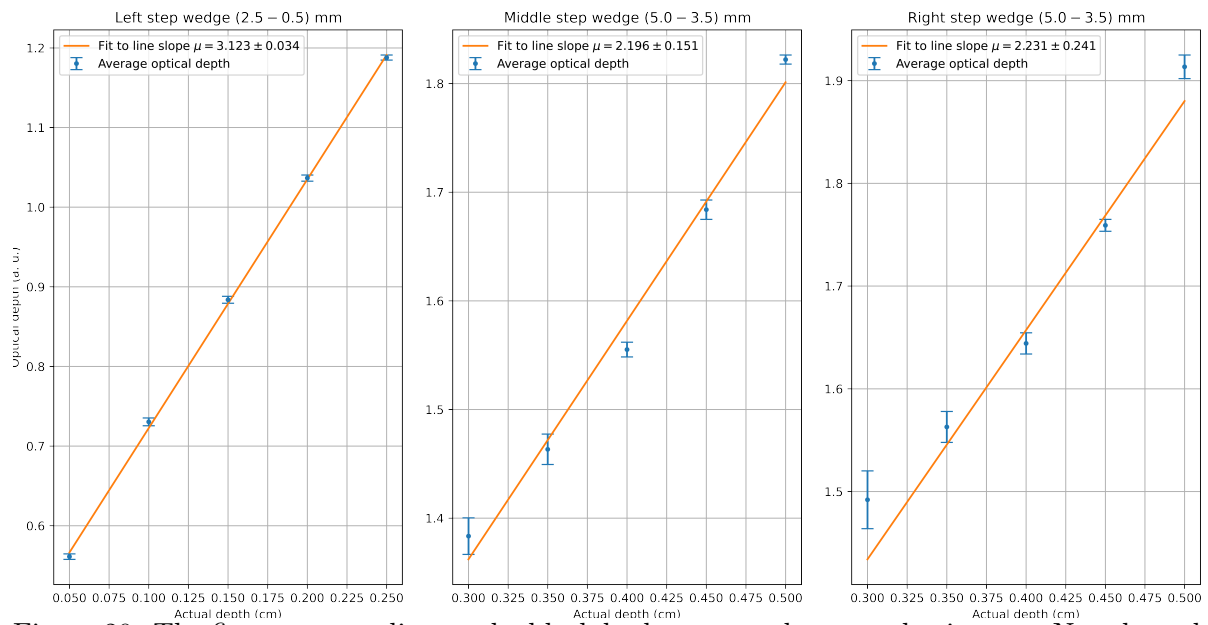


Figure 20: The fits corresponding to the black body corrected step wedge images. Note how the errors are smaller than in the previous calculation, which results from more removed background from the black body correction.

5.2 Washburn's equation and determining pore size

To determine the capillary rise a timeslice was made of each time series. This was done by finding sequence of images in the time series such that the shape of the wave front during the rise was easily recognizable and avoiding noise as well as possible. Then one could separate the already filled space from the unfilled/background space by applying a mask with the threshold of the waters optical thickness; getting just the already filled area back. An example of this is given in figure 21. One difficulty when choosing these slices, is that one either needs to find the start of the sequence (the capillary rise), or one needs to find a slice from which point the capillary rise is clearly visible. Here there was a temporary interruption in the beam when taking the data for slice 2, meaning that the slice had to be chosen in such a way that this interruption was not included. Additionally the slice needs to be done in such a way, that it terminates at the point where the entire sample is filled, for the fit to be accurate to the curve. All the slices were also chosen so that the areas of interest had a good SNR (see equation (4)), with the total SNR for the entire slices being about 2.5. This is not a high distinction against the background, but one should keep in mind that this is the *average* SNR for the entire image, meaning that it should tend to take on higher values in the areas of interest, where swaths of the background are excluded.

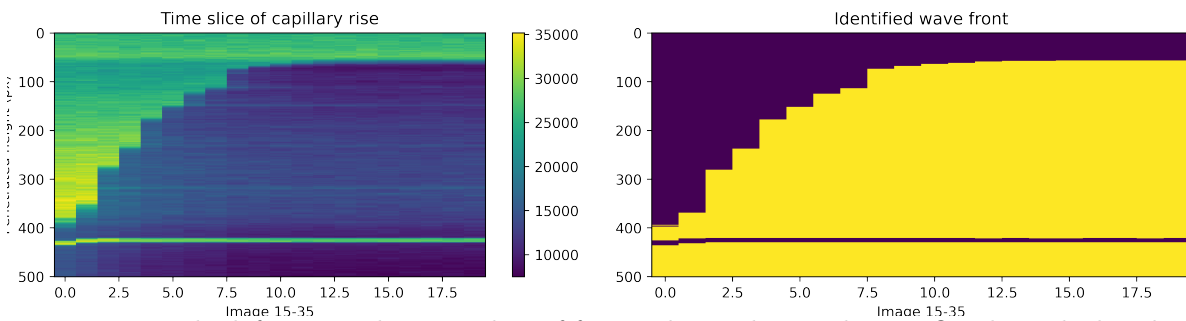


Figure 21: In the left image the time slice of for sand sample 3 is shown. On the right hand side is the mask determined via a histogram cutoff method, which is then used to find the height of the water column.

When this was done, one could easily find the highest point in each pillar, i.e. the highest position the wave front had reached. Had there been significant noise from the scintillator, one would maybe have had to take care not to get artificially inflated fronts. In the images taken by us, this was never an error, indicating that the noise from the additional photon emission of the scintillator would be relatively minimal.

When these had been extracted, one could convert the pixel values to cm by using the conversion factor found in 2¹. For the time-series normalization the image timestamps were found between the first and last image included in the slice. After this, all times

¹One should additionally note, due to the fact that a binning of 2x2 was used for this set of data, one needs to use twice the conversion factor to get the correct distance in cm.

were subtracted with the first, thus creating an array of time values giving the time passed since the start of the time lapse's slice to any image in the series; giving us a dataset of water-front propagation since the slice's beginning and the time stamps in second/minutes of the data points.

Now, if we were to perform a fit to equation (3), i.e. to the model:

$$L_{\text{Optical}}(t) = A\sqrt{t} + b \quad (5)$$

with A and b being the parameters to fit (again with b a parameter added for resilience against errors). With these fitted variables one can again compare with equation (3) and the values of all parameters except r from section 1 to extract the pore size with the following equation:

$$A = \sqrt{\frac{\gamma r \cos(\phi)}{2\eta}} \quad (6)$$

which with elementary algebraic manipulation gives us the following expression for r :

$$r = \frac{2A^2\eta}{\gamma \cos(\phi)} \quad (7)$$

In figure 22, such a fit as previously discussed, following equation (3) for the third sample (as seen in figure 21) is given.

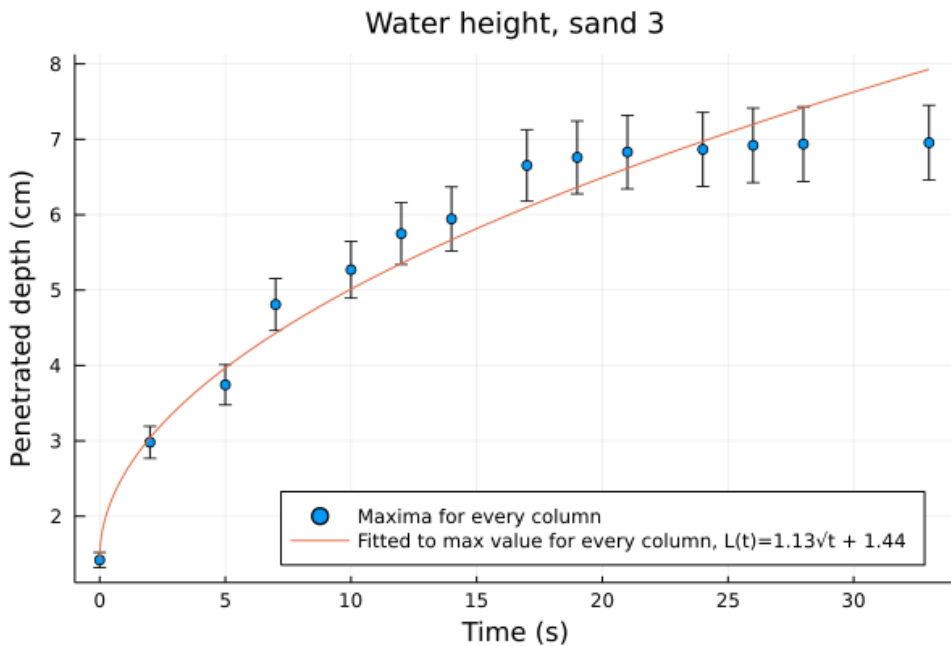


Figure 22: Caption

This was repeated for the remaining samples. Subsequently the analysis was repeated

again for the samples but the height of the water column was averaged instead of taken the max. This was done to provide a reference of the pore size less susceptible to noise. The results from these analyses can be found in table 3. The quality of the fits were all good, especially for the fit to the maximum values, where the χ^2/dof value was 1.83 ± 1.45 (three points). For the averaged points, the same value was 10.19 ± 12.95 . Here one should note the high error, meaning the fit qualities were widely spread (this is mainly a contribution from the fit of sample 2). In practice, this works as an endorsement of taking the maximum for every position.

Sand sample:	2 (0.1 – 0.2)mm	3 (0.1 – 3.2)mm	4 (0.4 – 0.8)mm
Pore size, highest water height [μm]:	(0.51 ± 0.03)	(4.91 ± 0.34)	(4.29 ± 0.49)
Pore size, average water height [μm]:	(0.74 ± 0.01)	(5.03 ± 0.24)	(6.0 ± 0.5)

Table 3: Different pore sizes for the different sand samples, calculated both using average water column height and maximal column height.

The values given in table 3 are reasonable, in [10] the average pore size of sand was given as between 1 and 100 μm , and that of fine sand between < 1 and 4 μm . This matches our results, as the result for sample 2, with grain sizes between 0.1 and 0.2 mm – fine sand – gives us about $(0.51 \pm 0.03) \mu\text{m}$ in pore size, matching that given in [10]. This also holds true for the fourth sample – an intermediary grain size – which situates itself above the 4 μm cutoff giving a pore size of $(4.29 \pm 0.49) \mu\text{m}$. This again corresponds nicely with the expected result.

A curious case is that of sample 3, giving us a similar sample size as sample 4 but with a much higher average grain size at $(4.91 \pm 0.34) \mu\text{m}$. One hypothesis which could explain this phenomenon is that the smaller grains in the sample permeate in the cavities left by the bigger grains; ultimately decreasing the effective pore size to that of the smaller grains. One flaw in this argumentation is that it should then take about the pore size of the smallest sample, 2. One possibility is that the central element of the mix is indeed slightly larger grains than sample 4, which we then would expect a slightly larger pore size. However, as we do not know the exact composition of the soil samples, a direct correspondence to the other two values can not be established, but presents an excellent opportunity for further studies.

It was planned to additionally extract the average water content pro position in the sample, bu due to the technical error the calibration images needed to get accurate images, including the black body images as well as the open beam and closed beam references.

6 Conclusion

In this experiment the linear attenuation of water was determined with and without black body correction to emphasize the usefulness of the imaging technique with an emphasis on what can be done to correct for unscattered contributions to the images. The attenuation coefficients were smaller than expected, which could have been a result of an inadequate re-scaling of the black body corrected image. Subsequently the capillary rise in three different samples were investigated, from which the average spore size was determined. These values were determined to be reasonable as previous research had already established similar values to those found.

A Safety

A.1 Controlled zones in PSI

In controlled zones as stipulated by Swiss law a dosimeter must be carried at all times and consumption of food is strictly prohibited as ingestion of radioactive isotopes far more dangerous than external exposure.

When leaving the controlled area, the person also needs to use a specialized tool to ensure that the person has not been contaminated.

A.2 Safety procedure when initiating the beam

When initiating the beam one must press a button inside and then complete clearing the area in 40 s. After clearing the experiment one first closes the experiment so that no one can enter it. Simultaneously a concrete block is shifted to completely cover the experiment.

When this is done, the beam can be engaged by opening the connection between the spallation source and the experiment area. Now the experiment is ready.

If one were to be trapped in the room when the beam initiated, one could also disengage it from inside the experiment using an emergency stop button.

A.3 Dangers inherent in the setup

Some materials used in the setup are heavy metals and as such harmful / carcinogenic to humans. Thus care should be taken when handling the setup to ensure that one does not interact with these elements without gloves or other safety equipment. To protect the operators from the beam, several thick concrete blocks surround the setup which is inaccessible while the beam is open.

References

- [1] Anders Kaestner. Real-time study of capillary rise in soil. <https://www.psi.ch/en/media/66534/download>. Accessed: 15.11.2021.
- [2] Chiara Carminati, Pierre Boillat, Florian Schmid, Peter Vontobel, Jan Hovind, Manuel Morgano, Marc Raventos, Muriel Siegwart, David Mannes, Christian Grünzweig, et al. Implementation and assessment of the black body bias correction in quantitative neutron imaging. *PLoS One*, 14(1):e0210300, 2019.
- [3] Marcus Mähring, Constança Tropa, and Anders Kaestner. Data analysis tutorial for capillary rise in soil at psi, Nov 2021. Interview per Zoom.
- [4] Becky Lavi, Abraham Marmur, and Joerg Bachmann. Porous media characterization by the two-liquid method: effect of dynamic contact angle and inertia. *Langmuir*, 24(5):1918–1923, 2008.
- [5] William R Leo. *Techniques for nuclear and particle physics experiments: a how-to approach*. Springer Science & Business Media, 2012.
- [6] Paul Scherrer Institut. Sinq: The swiss spallation neutron source. URL: <https://www.psi.ch/en/sinq>, accessed: 24.11.2021.
- [7] E. H. LEHMANN, P. VONTOBEL, and L. WIEZEL. Properties of the radiography facility neutra at sinq and its potential for use as european reference facility. *Nondestructive Testing and Evaluation*, 16(2-6):191–202, 2001.
- [8] P Boillat, C Carminati, F Schmid, C Grünzweig, J Hovind, A Kaestner, D Mannes, M Morgano, M Siegwart, P Trtik, et al. Chasing quantitative biases in neutron imaging with scintillator-camera detectors: a practical method with black body grids. *Optics express*, 26(12):15769–15784, 2018.
- [9] Andy Rowlands. *Physics of digital photography*. IOP Publishing, 2017.
- [10] Hideki Minagawa, Yasunori Nishikawa, Ikuko Ikeda, Kuniyuki Miyazaki, Naoya Takahara, Yasuhide Sakamoto, Takeshi Komai, and Hideo Narita. Characterization of sand sediment by pore size distribution and permeability using proton nuclear magnetic resonance measurement. *Journal of Geophysical Research: Solid Earth*, 113(B7), 2008.